DOI: 10.1002/adma.((please add manuscript number))

Article type: Communication

Efficient Semitransparent Solar Cells with High NIR Responsiveness Enabled by a Small-Bandgap Electron Acceptor

Feng Liu, Zichun Zhou, Cheng Zhang, Jianyun Zhang, Qin Hu, Thomas Vergot, Feng Liu, Thomas P. Russell, and Xiaozhang Zhu**

Feng Liu, Zichun Zhou, Cheng Zhang, Jianyun Zhang, Dr. Thomas Vergote, Prof. Xiaozhang Zhu*

Beijing National Laboratory for Molecular Sciences, CAS Key Laboratory of Organic Solids, Institute of Chemistry, Chinese Academy of Sciences, Beijing 100190, China
E-mail: xzzhu@iccas.ac.cn

Prof. Feng Liu*

Department of Physics and Astronomy, Shanghai Jiaotong University, Shanghai 200240, China

E-mail: fengliu82@sjtu.edu.cn

Feng Liu, Zichun Zhou, Cheng Zhang, Jianyun Zhang, Prof. Xiaozhang Zhu*

University of Chinese Academy of Sciences, Beijing 100049, China

Dr. Qin Hu, Prof. Feng Liu,

Materials Sciences Division, Lawrence Berkeley National Laboratory, Berkeley, CA 94720, United States

Prof. Thomas P. Russell

Polymer Science and Engineering Department, University of Massachusetts, Amherst, Massachusetts 01003, United States and Materials Sciences Division, Lawrence Berkeley National Laboratory, Berkeley, CA 94720, United States

Keywords: semitransparent organic solar cell, near infrared, non-fullerene acceptor, power conversion efficiency, thieno[3,4-*b*]thiophene

Significant progress has been achieved in the last decade in the field of bulk heterojunction (BHJ) organic photovoltaics (OPVs) with high power conversion efficiencies (PCEs) over 10%.[1] This progress can be attributed to the development of high-performance donor materials[2] designed with donor (D)–acceptor (A) or quinoidal strategies. To overcome the intrinsic defects of fullerene derivatives, such as weak absorption in the vis-near infrared (NIR) region, limited energy-level tunability, morphological instability, and high-cost production, non-fullerene electron acceptors (NFAs) featuring highly tunable optoelectronic properties by elegant chemical modifications have been developed as the new generation of electron acceptors in BHJ-OPVs.[3] The design of NFAs with complementary absorption and appropriate energy-level alignment matching with polymer donors is recognized as an effective way of achieving broad light absorption that can lead to higher OPV performance. Perylene diimide (PDI)-based NFAs with twisted backbones to restrain the strong self-aggregation tendency and to fine-tune the blend-film morphology have exhibited excellent photovoltaic performance.[4] Meng *et al.* have recently synthesized a three-dimensional (3D) PDI-based NFA, TPH-Se, with a large optical bandgap (E_g^{opt}) of 2.17 *e*V that, when combined with PDBT-T1 (E_g^{opt}: 1.85 *e*V) as the electron donor, yielded a promising PCE of 9.2%.[4a] Another kind of important NFA based on a planar A-D-A arrangement such as ITIC,[5] IEIC,[6] and IDTBR[7] show low-bandgap absorption and have

received even more attention.[8] By incorporating the methoxy group on the IEIC framework, Yao *et al.* synthesized a small-bandgap NFA, IEICO, with a long absorption edge at 925 nm (E_g^{opt}: 1.33 eV), that yielded a PCE of 8.4% with a high short-circuit current (J_{sc}) of 17.7 mA cm^{-2}.[9]

Inspired by the rapid development of OPVs, we can foresee commercial applications in the near future. One of the most promising applications is a semitransparent (ST) solar cell[10] that can be used in value-added applications in energy-harvesting windows. To date, most efforts in this area have been in the development of transparent electrodes with high transparency and conductivity, including graphene, metal nanowire networks or composites, conducting polymers, and thin metal films to realize STOPVs.[11] For the design of photovoltaic materials, it is a dilemma that more photons need to be harvested in the UV-vis-NIR region to generate a high current, but this reduces the transparency of the device. Recently, single-junction STOPVs utilizing fullerene acceptors showed relatively low PCEs of 4%–6% because of limited light absorption.[11a,11b,11e,11f,11i,11j,12] To enhance sunlight utilization, Chen *et al*. fabricated semitransparent tandem polymer solar cells (PSCs) by using two low-bandgap polymer donors, PBDTT-FDPP-C12 and PBDTT-SeDPP, that delivered a PCE of 7.3% with an average visible transmission ($T_{average}$) of 30%.[13] Thus, it is more challenging to achieve high-performance single-junction STOPVs that can only capture the incident light in a single pass.

The essence of designing STOPV materials and devices is to better utilize the NIR solar radiation and, meanwhile, keep open the 400–600 nm region, which is most sensitive to human vision. The maximum photopic (vision in bright light) human eye sensitivity is 555 nm and the maximum scotopic (vision in dim light) sensitivity is 507 nm. We believe that the emerging NFAs may provide a new opportunity to address this issue. By combining small-bandgap NFAs

with low-bandgap polymer donors, we can enhance the use of NIR solar irradiation, keep the eye-sensitive regions unblocked, and obtain high-performance single-junction STOPVs. We recently developed an electron acceptor (ATT-1) containing an effective thieno[3,4-*b*]thiophene and 2-(1,1-dicyanomethylene)rhodanine combination.[14] BHJ solar cells based on PTB7-Th and ATT-1 delivered high PCEs of up to 10.07%. However, the overlap absorption of PTB7-Th and ATT-1 limited the light absorption range. Herein, we designed and synthesized a small-bandgap electron acceptor (ATT-2) by introducing 2-(3-oxo-2,3-dihydroinden-1-ylidene)malononitrile with strong electron-accepting ability that can effectively decrease the lowest unoccupied molecular orbital (LUMO) energy levels and enhance intramolecular charge transfer. Thin films of ATT-2 show a broad absorption, ranging from 300 to 940 nm with an E_g^{opt} of 1.32 eV, which is 0.22 eV smaller than that of ATT-1 (1.54 eV). By combining with PTB7-Th, the as-cast OPVs yield PCEs of up to 9.58% with very high J_{sc} values of 20.75 mA cm^{-2}, an open-circuit voltage (V_{oc}) of 0.73 V, and fill factor (FF) of 0.63. Compared with the thiophene counterpart, IEIC (V_{oc}: 0.97 V; J_{sc}: 13.55 mA cm^{-2}; FF: 0.48; PCE: 6.31%),[6] the high J_{sc} and FF of ATT-2 can sufficiently compensate for the V_{oc} loss to achieve significantly improved device performance. Furthermore, ATT-2 and PTB7-Th form complementary absorption in the NIR region, which is beneficial in achieving high-performance STOPVs. By using a thin Ag anode, STOPVs had PCEs of up to 7.74% with a J_{sc} of 18.53 mA cm^{-2} and a $T_{average}$ of 37%, which to date is the highest reported PCE value for single-junction STOPVs.

The synthesis of the ATT-2 compound is shown in **Figure 1**. A Stille-type crosscoupling of octyl 6-bromo-4-formylthieno[3,4-*b*]thiophene-2-carboxylate **1**[15] and (4,4,9,9-tetrakis(4-hexylphenyl)-4,9-dihydro-s-indaceno[1,2-*b*:5,6-*b*']dithiophene-2,7-diyl)bis(trimethylstannane) **2** gave dialdehyde **3,** which then reacted with (dicyanomethylene)indent-1-one to give the

target molecule ATT-2 with 84% yield as a dark-green solid. ATT-2 shows excellent thermal stability (up to 335 °C with 5% weight loss) (**Figure S1**) and can be dissolved in common organic solvents such as chloroform and chlorobenzene at room temperature, which ensures its solution processability.

The UV-vis-NIR absorption spectra of ATT-2 were examined in chloroform and thin films (**Figure 2a**). The chloroform solution of ATT-2 showed a strong absorption in the 600–850 nm region with a high molar absorption coefficient of 2.0 $\times 10^5$ L mol^{-1} cm^{-1} at 791 nm (**Figure S2**). The ATT-2 thin film showed a maximum absorption at 835 nm, which was significantly red-shifted by 45 nm. The E_g^{opt} of ATT-2 was determined to be 1.32 eV based on the absorption onset in thin film at 940 nm. The electrochemical properties of the ATT-2 thin films were examined by cyclic voltammetry (see **Figure S3)**. The HOMO and LUMO energy levels of ATT-2 and PTB7-Th were estimated to be –5.50 and –3.90 eV, respectively, based on the onsets of the oxidation and reduction curves [$E_{HOMO/LUMO} = -(4.80 + E_{ox/red}^{onset})$ eV].

PTB7-Th is a high-performance donor material.[16] We selected PTB7-Th as the electron donor for two reasons: i) the ΔE_{LUMO} and ΔE_{HOMO} values between PTB7-Th and ATT-2 blends were both 0.30 eV, which provides favorable energetic offsets for exciton dissociation; and ii) the absorption spectra of the PTB7-Th thin films exhibit a low-bandgap absorption in the region of 550–750 nm, which can form complementary absorption with our ATT-2 electron acceptor in the NIR region of 600–940 nm in blend films (**Figure 2a**, **S4**). The complementary absorption spectra of PTB7-Th and ATT-2 are beneficial in enhancing light harvesting, so as to increase J_{sc}. To demonstrate the potential of the small-bandgap ATT-2 as an electron acceptor, we fabricated BHJ-OPVs in an inverted device configuration of ITO/ZnO/PTB7-Th:ATT-2/MoO_3/Ag, where

ZnO and MoO_3 were applied individually as the cathode and anode interlayers. **Table 1** summarizes the photovoltaic parameters for devices with and without 1-chloronaphthalene as solution additives. The current-density/voltage (*J*–*V*) curves corresponding to the best PCEs under simulated AM 1.5 G, 100 mW cm^{-2} irradiance are shown in **Figure 3a**. OPV devices with a 1:1.8 PTB7-Th/ATT-2 weight ratio showed an optimized average PCE of 4.87% with a J_{sc} value of 12.85 mA cm^{-2}, a V_{oc} value of 0.74 V, and a FF of 50%. 1-Chloronaphthalene (1-CN), as an aromatic processing additive, was firstly utilized by Coffin *et al.* to improve the intermixing of the electron donor and acceptor phases giving much improved PCE.[18] With addition of 2% 1-chloronaphthalene (CN), the PCEs of ATT-2 could be enhanced to 9.58%, with a high J_{sc} of 20.75 mA cm^{-2}, a V_{oc} of 0.73 V, and FF of 63%. The photon energy loss (E_{loss}) was estimated to be 0.59 eV according to $E_{loss} = E_g - eV_{oc}$. Compared with the devices with an active area of 3.08 mm^2, OPV devices with a larger active area of 0.1 cm^2 were fabricated and showed a similarly high PCE of 9.42% with a J_{sc} of 20.55 mA/cm^2 (**Figure S5**). The corresponding incident photon to converted current efficiency (IPCE) spectra for solar cells with and without 2% CN as an additive are shown in **Figure 3b**. The J_{sc} value, calculated from the integration of the IPCE spectrum was 19.8 mA cm^{-2}, which agreed well with the J_{sc} value obtained from the *J*–*V* curves with a 5% deviation. The devices based on the combination of PTB7-Th with ATT-2 showed a broad IPCE spectrum response in the regions of 300–940 nm, suggesting that both the polymer donor and the small-molecule acceptor make considerable contributions to J_{sc}. The IPCE values of the optimized PTB7-Th:ATT-2 blend were above 50% in the wavelength range of 485–865 nm with the maximum value approaching 72%, which indicates efficient photon harvesting and charge collection. For comparison, we also fabricated ATT-1/PTB7-Th-based OPV devices with the inverted configuration of ITO/ZnO/PTB7-Th:ATT-1/MoO_3/Ag. Under the optimized conditions,

ATT-1-based solar cells showed a relatively low PCE of 5.47%, with a V_{oc} of 0.92 V, a J_{sc} of 12.94 mA cm^{-2}, and a FF of 46.0. By 1-CN treatment, the device performance was only slightly improved to a similar PCE of 5.69% with a V_{oc} of 0.92 V, a J_{sc} of 13.3 mA cm^{-2}, and FF of 46.5. We examined the ambient stability of the ATT-2-based OPV devices without encapsulation, which indicates that after an initial drop from 9.4% to 8.8% within 48 hrs, the PCE kept stable for at least 14 days (**Figure S6**).

The charge transport properties of the optimized PTB7-Th:ATT-2 blend film were investigated by the space-charge-limited current (SCLC) method with the device configurations of Al/PTB7-Th:ATT-2/Al for electron and ITO/PEDOT:PSS/PTB7-Th:ATT-2/MoO_3/Ag for hole transport measurements (see **Figure S7**). The hole- and electron-mobility values of the as-cast PTB7-Th:ATT-2 film were found to be μ_h: 0.73 $\times 10^{-4}$ cm^2 V^{-1} s^{-1} and μ_e: 1.18 $\times 10^{-4}$ cm^2 V^{-1} s^{-1} with a μ_h/μ_e ratio of 0.61. After the addition of 2 wt% 1-CN, the hole and electron mobility increased to μ_h: 5.10 $\times 10^{-4}$ cm^2 V^{-1} s^{-1} and μ_e: 3.69 $\times 10^{-4}$ cm^2 V^{-1} s^{-1} with a μ_h/μ_e ratio of 1.38. The high and balanced charge transport property of the 1-CN-treated blend film was responsible for the high J_{sc} and FF values.

To gain insight into exciton dissociation, the relationship between photocurrent density (J_{ph}) and effective voltage (V_{eff}) was investigated (**Figure 3c**). The value of J_{ph} is defined as J_L–J_D, where J_L and J_D are the current densities under illumination and in dark conditions, respectively. The term V_{eff} is defined by V_0–V,[17] where V_0 is the voltage when J_{ph} = 0 and V is the applied voltage. For the optimized device, the value of J_{ph} reached its saturation (J_{sat}) when the value of V_{eff} was close to 1.9 V, where all the photogenerated excitons dissociated into free charge carriers and were collected by the electrodes. The charge dissociation probability P (E,T) is

defined as J_{ph}/J_{sat}, yielding 82% and 94% for the as-cast blend film and for the blend film treated with 2% 1-CN, respectively, which indicates the efficient exciton dissociation in the 1-CN-treated solar cells. Furthermore, we measured the correlation between J_{sc} and light intensity to evaluate the charge recombination behavior affecting device performance.[19] The correlation between J_{sc} and light intensity can be addressed by the formula $J_{sc} \propto P^{\alpha}$, where α should be equal to 1 when all the free carriers are swept out and collected at the electrodes with negligible bimolecular recombination. As shown in **Figure 3d**, the α values of the device based on PTB7-Th:ATT-2 blend film with and without 1-CN were determined to be 0.95 and 0.88, respectively. As a consequence, the efficient exciton dissociation and negligible bimolecular recombination led to an extremely high J_{sc} in 1-CN-treated OPVs. The steady-state photoluminescence (PL) spectra of the neat ATT-2 film and the blend film of ATT-2:PTB7-Th are shown in **Figure S8**. For the blend film, the PL emission of PTB7-Th (excited at 700 nm) was completely quenched by ATT-2, and meanwhile no emission from ATT-2 was observed, indicating efficient electron transfer from polymer donor PTB7-Th to electron acceptor ATT-2.

The crystalline order of pure materials and the BHJ blends were characterized by grazing incidence x-ray diffraction (GIXD) (**Figure 4a–b**). PTB7-Th showed a face-on orientation with π–π stacking at 1.60 $Å^{-1}$ (0.39 nm) and a (100) diffraction peak at 0.27 $Å^{-1}$ (2.32 nm). The ATT-2 film showed a (100) diffraction peak at 0.31 $Å^{-1}$ (2.02 nm) and a π–π stacking region at 1.80 $Å^{-1}$ (0.35 nm). The blended film contained structural features of both PTB7-Th and ATT-2. In the as-cast film, the (100) peak and π–π stacking regions have broadened. The similarity of PTB7-Th and ATT-2 scattering features make it hard to differentiate between the scattering peaks. When the 1-CN additive was used, the scattering profiles changed significantly. The in-plane direction was dominated by a sharp ATT-2 (100) peak and the out-of-plane direction by an ATT-2 π–π

stacking peak. The ATT-2 (100) coherence length was estimated to be 22.2 nm; the ATT-2 π–π stacking coherence length was estimated to be 7.3 nm. Thus, the 1-CN additive could significantly enhance the self-assembly of ATT-2 and its transport properties. The PTB7-Th features in 1-CN-processed blends were shadowed by ATT-2. The phase separation in the BHJ thin film was investigated by resonant soft x-ray scattering (RSoXS). The as-cast thin film showed a scattering peak at 0.0033 $Å^{-1}$, corresponding to a distance of 190 nm. Adding 1-CN drastically shifted the scattering peak to 0.013 $Å^{-1}$, giving a distance of 48 nm. The significant reduction in the characteristic length scale suggests the formation of a finer bicontinuous network structure, which would significantly enhance J_{sc} in the optimized devices. The surface morphology of the PTB7-Th:ATT-2 blend films was investigated using atomic force microscopy (AFM). Adding 1-CN reduced the large aggregates in the thin film and reduced the surface roughness in agreement with scattering results (**Figure S9**).

Encouraged by the complementary absorption of PTB7-Th and ATT-2 in the NIR region, we further demonstrated the STOPVs by using thin Ag electrodes. Ag electrode possesses high work function with air stability, the long skin-depth facilitating photon penetration,[11b] and, especially, the reduced transmittance in the NIR region compared with that in the visible region,[11i] which matches well with our idea of enhancing the utilization of NIR light and transmitting more visible light. The transmission spectra, the *J*–*V* curves, and the relevant parameters of the optimized devices are shown in **Figure 5** and summarized in **Table 1**. By gradually reducing the thickness of the Ag electrode from 20 nm to 5 nm, the average visible transmittance of the devices increased from 37% to 48% (Figure 5b). The reduced reflectivity of the thin anode electrode reduced light intensity in the active layer, which led to a smaller J_{sc}. When an ultrathin (10 nm) Ag electrode was used, the semitransparent device showed good

average visible transmittance, AVT ($T_{average}$), of 45% with a PCE of 6.3% and J_{sc} of 16.01 mA cm^{-2}. When the Ag thickness was increased to 20 nm, the AVT decreased to 37% with a PCE of 7.74% and J_{sc} of 18.53 mA cm^{-1}. The 350–600 nm region was highly transparent at different Ag thickness values, which is particularly interesting for STOPV applications. Such a large spectral window covers the maximum photopic and scotopic sensitivity of the human eye (**Figure 5c**), and can be used in both high-light and low-light conditions. **Figure 5d** presents a colorful printed picture with and without the STOPV window. The blue, green, and orange colored letters remain of a similar color when the device window was applied. The red letter became darker, as this overlaps with the BHJ thin film absorption. This color distortion was small because the transparency at 600 nm was still above 20% for the 20 nm Ag device. In Figure S10, ATT-2:PTB7-Th blend films with Ag electrodes of different thickness showed much higher transmission than those of ATT-1:PTB7-Th blend film. Compared with ATT-1, the small-bandgap ATT-2 is more suitable STOPV applications in terms of its enhanced absorption in NIR region and reduced absorption in visible region. The Commission Internationale de l'Eclairage (CIE) 1931 color coordinates, correlative color temperature (CCT) and color rendering index (CRI) of the STOPV device with 20 nm Ag electrode were calculated (**Figure S12**). The STOPV device had a CIE color coordinates of (0.2805, 0.3076), a CCT of 9113 K, and showed an excellent CRI of 94.1, which means the good color rendering property of the ATT-2:PTB7-Th-based STOPVs. Thus, this new type of STOPV can be of high potential for photonic energy windows that can be integrated into building materials. When new transparent electrodes are used, the performance could be further improved.

In summary, we have developed a new, deep-absorbing, small-bandgap electron acceptor material ATT-2 for non-fullerene STOPV applications. The light absorption and frontier orbital

energy levels fit well with many high-performance electron-donating polymers and small molecules. It is thus of high value for harvesting deep wavelength solar radiation. By combining ATT-2 with the low-bandgap polymer PTB7-Th, the absorption window could be pushed into the NIR region, resulting in a high PCE of 9.58% for opaque OPVs and 7.74% for single-junction STOPVs. The blue–green–orange spectral range of the STOPVs was highly transparent. Although fullerene derivatives have been frequently used in STOPVs, the fullerene absorption covered the green region, enlarging the color distortion. The current proof-of-concept device showed good improvements in transparency in the visible region and the best STOPV performance. Thus, non-fullerene acceptors should be very promising for the development of high-performance STOPVs.[20]

Supporting Information

Supporting Information is available online from the Wiley Online Library or from the author.

Acknowledgements

F.L. and Z.Z. contributed equally to this work. We thank the National Basic Research Program of China (973 Program) (No. 2014CB643502) for financial support, the Strategic Priority Research Program of the Chinese Academy of Sciences (XDB12010200), and the National Natural Science Foundation of China (91333113, 21572234). F.L. was supported by the Young 1000 Talents Global Recruitment Program of China. T.P.R. was supported by the U.S. Office of Naval Research under contract N00014-15-1-2244. Portions of this research were carried out at beamline 7.3.3 and 11.0.1.2 at the Advanced Light Source, Molecular Foundry, and National Center for Electron Microscopy, Lawrence Berkeley National Laboratory, which was supported by the DOE, Office of Science, and Office of Basic Energy Sciences.

Received: ((will be filled in by the editorial staff))
Revised: ((will be filled in by the editorial staff))
Published online: ((will be filled in by the editorial staff))

[1] a) J. Zhao, Y. Li, G. Yang, K. Jiang, H. Lin, H. Ade, W. Ma, H. Yan, *Nature Energy* **2016**, *1*, 15027; b) S. Zhang, L. Ye, W. Zhao, B. Yang, Q. Wang, J. Hou, *Sci. China Chem.* **2015**, *58*, 248; c) V. Vohral, K. Kawashima, T. Kakara, T. Koganezawa, I. Osaka, K. Takimiya, H. Murata, *Nature Photon.* **2015**, *9*, 403; d) B. Kan, Q. Zhang, M. Li, X. Wan, W. Ni, G. Long, Y. Wang, X. Yang, H. Feng, Y. Chen, *J. Am. Chem. Soc.* **2014**, *136*, 15529.

[2] L. Lu, T. Zheng, Q. Wu, A. M. Schneider, D. Zhao, L. Yu, *Chem. Rev.* **2015**, *115*, 12666.

[3] a) Y. Lin, X. Zhan, *Mater. Horiz.* **2014**, *1*, 470; b) C. B. Neilsen, S. Holliday, H.-Y. Chen, S. Cryer, I. McCulloch, *Acc. Chem. Soc.* **2015**, *48*, 2803; c) Y. Lin, X. Zhan, *Acc. Chem. Res.* **2016**, *49*, 175.

[4] a) D. Meng, H. Fu, C. Xiao, X. Meng, T. Winands, W. Ma, W. Wei, B. Fan, L. Huo, N. Doltsinis, Y. Li, Y. Sun, Z. Wang, *J. Am. Chem. Soc.* **2016**, *138*, 10184; b) Q. Wu, D. Zhao, A. M. Schneider, W. Chen, L. Yu, *J. Am. Chem. Soc.* **2016**, *138*, 7248; c) H. Zhong, C.-H. Wu, C.-Z. Li, J. Carpenter, C.-C. Chueh, J.-Y. Chen, H. Ade, A. K.-Y. Jen, *Adv. Mater.* **2016**, *28*, 951; d) Y.-J. Hwang, H. Li, B. A. E. Courtright, S. Subramaniyan, S. A. Jenekhe, *Adv. Mater.* **2016**, *28*, 124; e) Y. Zhong, M. T. Trinh, R. Chen, G. E. Purdum, P. P. Khlyabich, M. Sezen, S. Oh, H. Zhu, B. Fowler, B. Zhang, W. Wang, C.-Y. Nam, M. Y. Sfeir, C. T. Black, M. L. Steigerwald, Y.-L. Loo, F. Ng, X.-Y. Zhu, C. Nuckolls, *Nat. Commun.* **2015**, *6*, 8242; f) J. Liu, S. Chen, D. Qian, B. Gautam, G. Yang, J. Zhao, J. Bergqvist, F. Zhang, W. Ma, H. Ade, O. Inganäs, K. Gundogdu, G. Gao, H. Yan, *Nature Energy* **2016**, *1*, 16089.

[5] Y. Lin, J. Zhao, Z.-G. Zhang, H. Bai, Y. Li, D. Zhu, X. Zhan, *Adv. Mater.* **2015**, *27*, 1170.

[6] Y. Lin, Z.-G. Zhang, H. Bai, J. Wang, Y. Yao, Y. Li, D. Zhu, X. Zhan, *Energy Environ. Sci.* **2015**, *8*, 610.

[7] S. Holliday, R. Ashraf, A. Wadsworth, D. Baran, S. Yousaf, C. Nielsen, C.-H. Tan, S. Dimitrov, Z. Shang, N. Gasparini, M. Alamoudi, F. Laquai, C. Brabec, A. Salleo, J. Durrant, I. McCulloch, *Nat. Commun.* **2016**, *7*, 11585.

[8] a) W. Zhao, D. Qian, S. Zhang, S. Li, O. Inganas, F. Gao, J. Hou, *Adv. Mater.* 2016, 28, 4734; b) Y. Lin, F. Zhao, Q. He, L. Huo, Y. Wu, T. C. Parker, W. Ma, Y. Sun, C. Wang, D. Zhu, A. J. Heeger, S. R. Marder, X. Zhan, *J. Am. Chem. Soc.* **2016**, *138*, 4955; c) Y. Yang, Z.-G. Zhang, H. Bin, S. Chen, L. Gao, L. Xue, C. Yang, Y. Li, *J. Am. Chem. Soc.* **2016**, DOI: 10.1021/jacs.6b09110; d) H. Lin, S. Chen, Z. Li, J. Y. L. Lai, G. Yang, T. McAfee, K. Jiang, Y. Li, H. Hu, J. Zhao, W. Ma, H. Ade, H. Yan, *Adv. Mater.* **2015**, *27*, 7299; e) Y. Li, L, Zhong, F.-P. Wu, Y. Yuan, H.-J. Bin, Z.-Q. Jiang, Z. Zhang, Z.-G. Zhang, Y. Li, L.-S. Liao, *Energy Environ. Sci.* **2016**, *9*, 3429; f) Y. Li, D. Qian, L. Zhong, J.-D. Lin, Z.-Q. Jiang, Z.-G. Zhang, Z. Zhang, Y. Li, L.-S. Liao, F. Zhang, *Nano Energy* **2016**, *27*, 430; g) M. Li, Y. Liu, W. Ni, F. Liu, H. Feng, Y. Zhang, T. Liu, H. Zhang, X. Wan, B. Kan, Q. Zhang, T. P. Russell, Y. Chen, *J. Mater. Chem. A.* **2016**, *4*, 10409; h) N. Liu, H. Zhang, X. Wan, C. Li, X. Ke, H. Feng, B. Kan, H. Zhang, Q. Zhang, Y. Lu, Y. Chen, *Adv. Mater.* **2016**, DIO: 10.1002/adma.201604964. (i) S. Dai, F. Zhao, Q. Zhang, T.-K. Lau, T. Li, K. Liu, Q. Ling, C. Wang, X. Lu, W. You, X. Zhan, *J. Am. Chem. Soc.*, **2017**, *139*, 1336; (j) Y. Lin, F. Zhao, Y. Wu, K. Chen, Y. Xia, G. Li, S. K. K. Prasad, J. Zhu, L. Huo, H. Bin, Z.-G. Zhang, X. Guo, M. Zhang, Y. Sun, F. Gao, Z. Wei, W. Ma, C. Wang, J. Hodgkiss, Z. Bo, O. Inganäs, Y. Li, X. Zhan, *Adv. Mater.*, **2017**, 29, 1604155; (k) P. Cheng, M. Zhang, T.-K. Lau, Y. Wu, B. Jia, J. Wang, C. Yan, M. Qin, X. Lu, X. Zhan, *Adv. Mater.* **2016**, DOI: 10.1002/adma. 201605216; (l) Y. Lin, T. Li, F. Zhao, L. Han, Z. Wang, Y. Wu, Q. He, J. Wang, L. Huo, Y. Sun, C. Wang, W. Ma, X. Zhan, *Adv.*

Energy Mater. **2016**, *6*, 1600854; (m) Y. Lin, Q. He, F. Zhao, L. Huo, J. Mai, X. Lu, C.-J. Su, T. Li, J. Wang, J. Zhu, Y. Sun, C. Wang, X. Zhan, *J. Am. Chem. Soc.* **2016**, *138*, 2973.

[9] H. Yao, Y. Chen, Y. Qin, R. Yu, Y. Cui, B. Yang, S. Li, K. Zhang, J. Hou, *Adv. Mater.* **2016**, *28*, 8283.

[10] P. Romero-Gómez, F. Pastorelli, P. Mantilla-Pérez, M. Mariano, A. Martínez-Otero, X. Elias, R. Betancur, J. Martorell, *J. Photon. Energy* **2015**, *5*, 057212.

[11] a) C.-C. Chen, L. Dou, R. Zhu, C.-H. Chung, T.-B. Song, Y. B. Zheng, S. Hawks, G. Li, P. S. Weiss, Y. Yang, *ACS Nano* **2012**, *6*, 7185; b) C.-C. Chueh, S.-C. Chien, H.-L. Yip, J.-F. Salinas, C.-Z. Li, K.-S. Chen, F.-C. Chen, W.-C. Chen, A. K.-Y. Jen, *Adv. Energy Mater.* **2012**, *3*, 417; c) Z. Tang, Z. George, Z. Ma, J. Bergqvist, K. Tvingstedt, K. Vandewal, E. Wang, L. M. Andersson, M. R. Andersson, F. Zhang, O. Inganäs, *Adv. Energy Mater.* **2012**, *2*, 1467; d) E. C. Garnett, W. Cai, J. J. Cha, F. Mahmood, S. T. Connor, M. G. Christoforo, Y. Cui, M. D. McGehee, M. L. Brongersma, *Nat. Mater.* **2012**, *11*, 241; e) J. Czolk, A. Puetz, D. Kutsarov, M. Reinhard, U. Lemmer, A. Colsmann, *Adv. Energy Mater.* **2013**, *3*, 386; f) F. Guo, X. Zhu, K. Forberich, J. Krantz, T. Stubhan, M. Salinas, M. Halik, S. Spallek, B. Butz, E. Spiecker, T. Ameri, N. Li, P. Kubis, D. M. Guldi, G. J. Matt, C. J. Brabec, *Adv. Energy Mater.* **2013**, *3*, 1062; g) A. R. b. M. Yusoff, S. J. Lee, F. K. Shneider, W. J. da Silva, J. Jang, *Adv. Energy Mater.* **2014**, *4*, 1301989; h) C.-Y. Chang, L. Zuo, H.-L. Yip, C.-Z. Li, Y. Li, C.-S. Hsu, Y.-J. Cheng, H. Chen, A. K. Y. Jen, *Adv. Energy Mater.* **2014,** *4*, 1301645; i) X. Ren, X. Li, W. C. H. Choy, *Nano Energy* **2015**, *17*, 187; j) Y. Song, S. Chang, S. Gradecak, J. Kong, *Adv. Energy Mater.* **2016**, *6*, 1600847.

[12] a) Z. M. Beiley, M. G. Christoforo, P. Gratia, A. R. Bowring, P. Eberspacher, G. Y. Margulis, C. Cabanetos, P. M. Beaujuge, A. Salleo, M. D. McGehee, *Adv. Mater.* **2013**, *25*, 7020; b) C.-Y. Chang, L.

Zuo, H.-L. Yip, Y. Li, C.-Z. Li, C.-S. Hsu, Y.-J. Cheng, H. Chen, A. K. Y. Jen, *Adv. Funct. Mater.* **2013**, *23*, 5084; c) M. Zhang, X. Guo, W. Ma, H. Ade, J. Hou, *Adv. Mater.* **2015**, *27*, 4655.

[13] C.-C. Chen, L. Dou, J. Gao, W.-H. Chang, G. Li, Y. Yang, *Energy Environ. Sci.* **2013**, *6*, 2714.

[14] F. Liu, Z. Zhou, C. Zhang, T. Vergote, H. Fan, F. Liu, X. Zhu, *J. Am. Chem. Soc.* **2016**, DOI: 10.1021/jacs.6b08523.

[15] F. Liu, G. L. Espejo, S. Qiu, M. M. Oliva, J. Pina, J. S. S. de Melo, J. Casado, X. Zhu, *J. Am. Chem. Soc.* **2015**, *137*, 10357.

[16] S.-H. Liao, H.-J. Jhuo, Y.-S. Cheng, S.-A. Chen, *Adv. Mater.* **2013**, *25*, 4766.

[17] P. W. M. Blom, V. D. Mihailetchi, L. J. A. Koster, D. E. Markov, *Adv. Mater.* **2007**, *19*, 1551.

[18] R. C. Coffin, J. Peet, J. Rogers, G. C. Bazan, *Nature Chem.* **2009**, *1*, 657.

[19] a) I. Riedel, J. Parisi, V. Dyakonov, L. Lutsen, D. Vanderzande, J. C. Hummelen, *Adv. Funct. Mater.* **2004**, *14*, 38; b) S. R. Cowan, A. Roy, A. Heeger, *J. Phys. Rev. B* **2010**, *82*, 245207.

[20] Lunt, R. R. *App. Phys. Lett.* **2012**, 101, 043902.

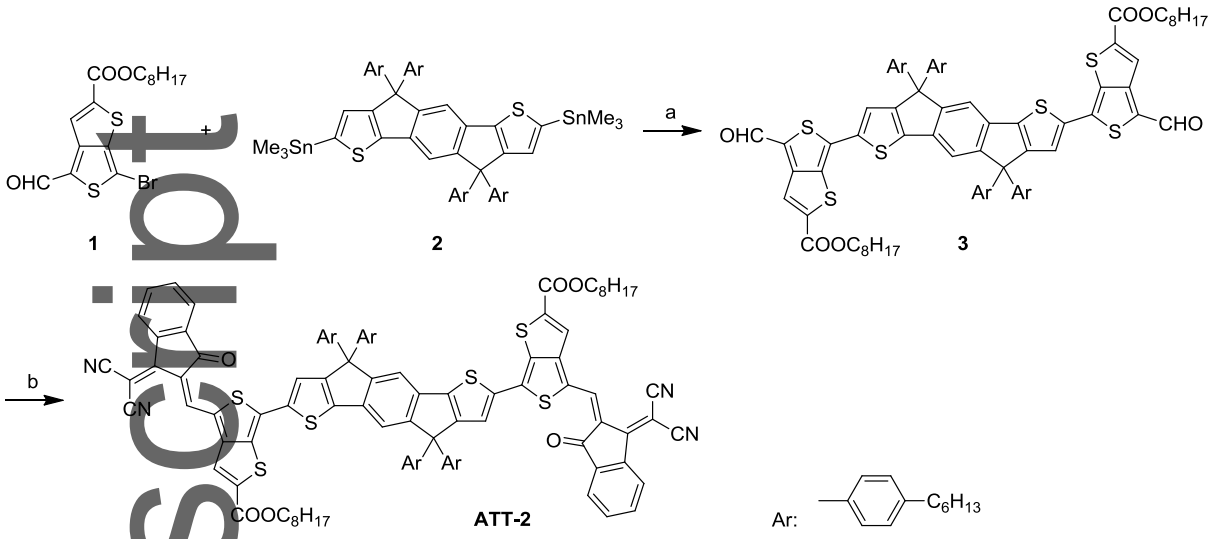

Figure 1. Synthesis of ATT-2. Reagents and conditions: (a) $Pd(PPh_3)_4$, toluene, reflux; (b) 3-(dicyanomethylidene)indan-1-one, pyridine, chloroform, reflux.

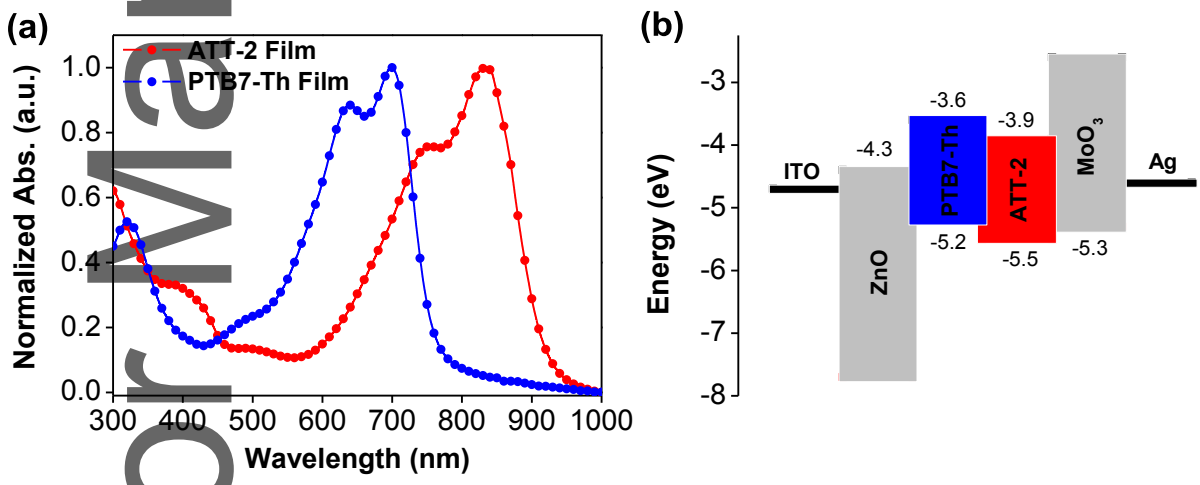

Figure 2. (a) The normalized UV-vis-NIR absorption spectra of PTB7-Th and ATT-2 in thin films; (b) schematic energy diagrams of ZnO, PTB7-Th, ATT-2, and MoO_3.

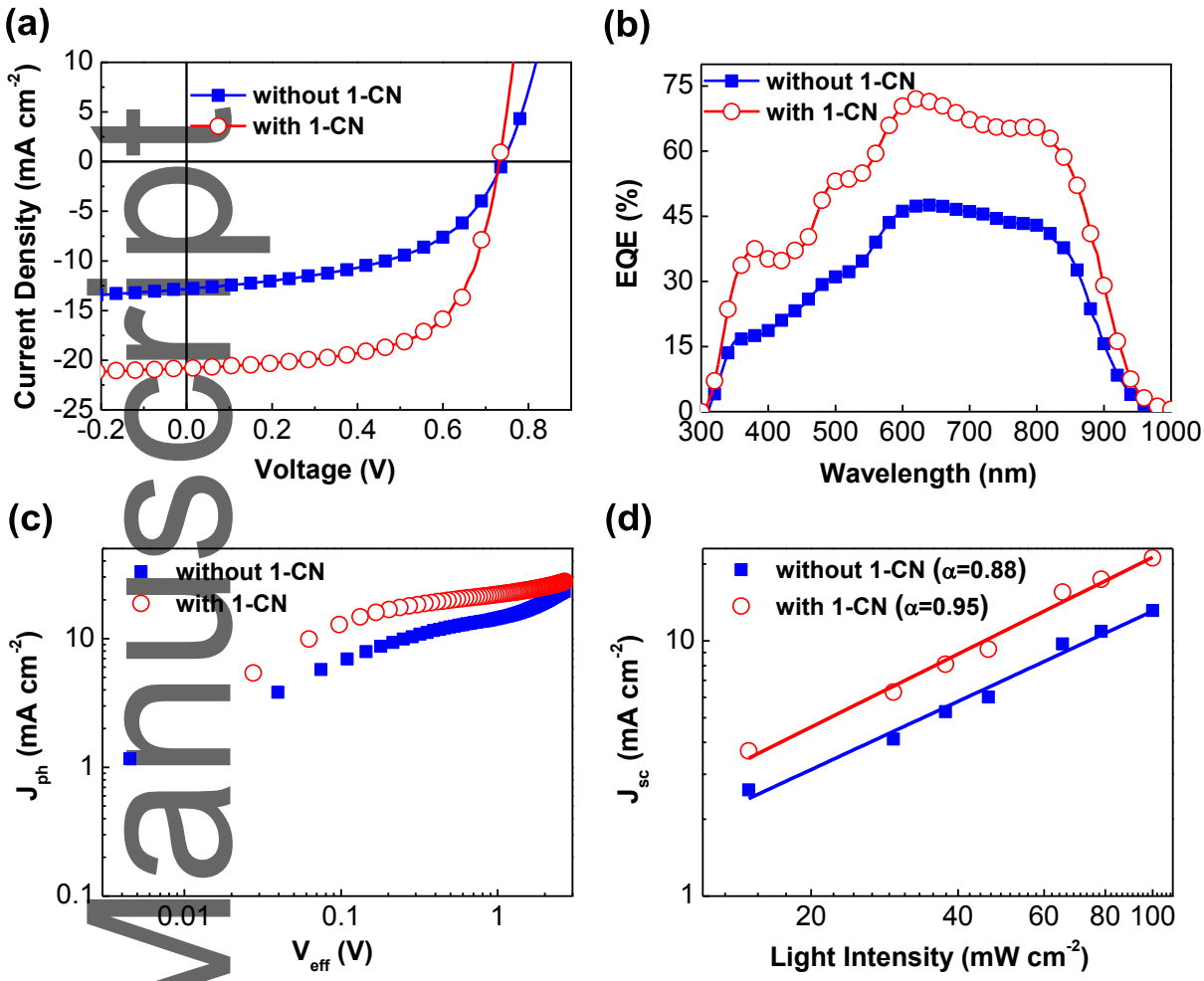

Figure 3. (a) Characteristic density vs voltage (*J*–*V*) curves and (b) external quantum efficiency (EQE) curves for the optimized devices under AM 1.5 G irradiation (100 mW cm^{-2}). (c) J_{ph} vs V_{eff} characteristics. (d) J_{sc} as a function of light intensity.

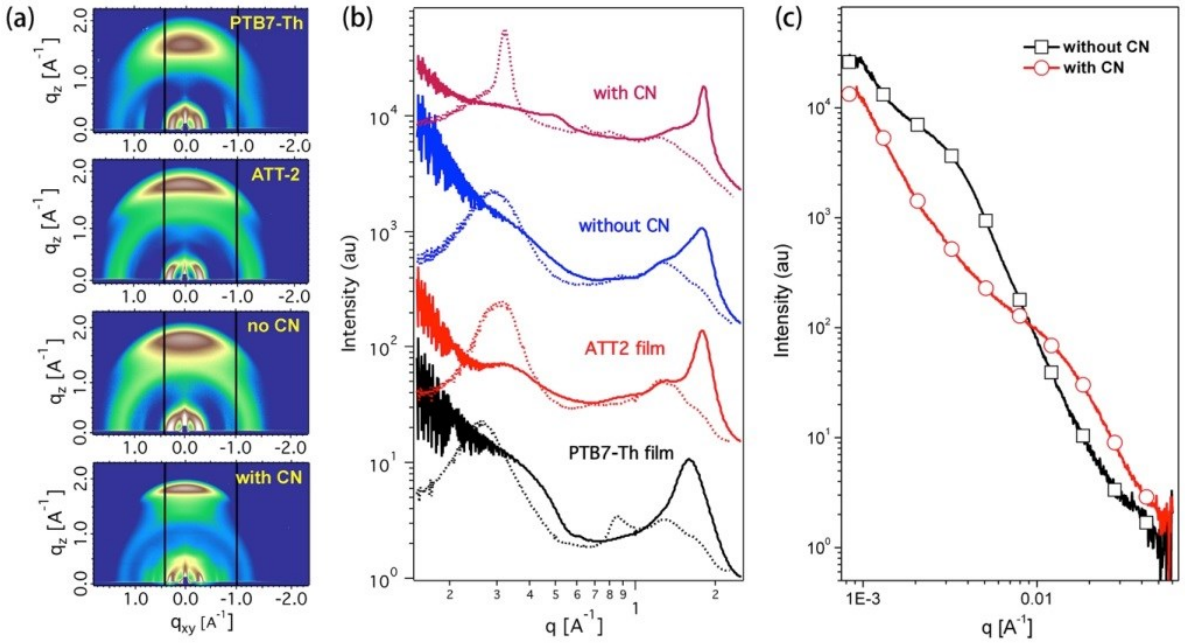

Figure 4. (a) 2D GIXD diffraction images of the pristine and PTB7-Th:ATT-2 blend films; (b) in-plane (dotted line) and out-of-plane (solid line) x-ray scattering profiles extracted from the 2D GIXD images. (c) RSoXS profiles for PTB7-Th:ATT-2 blend films with/without CN.

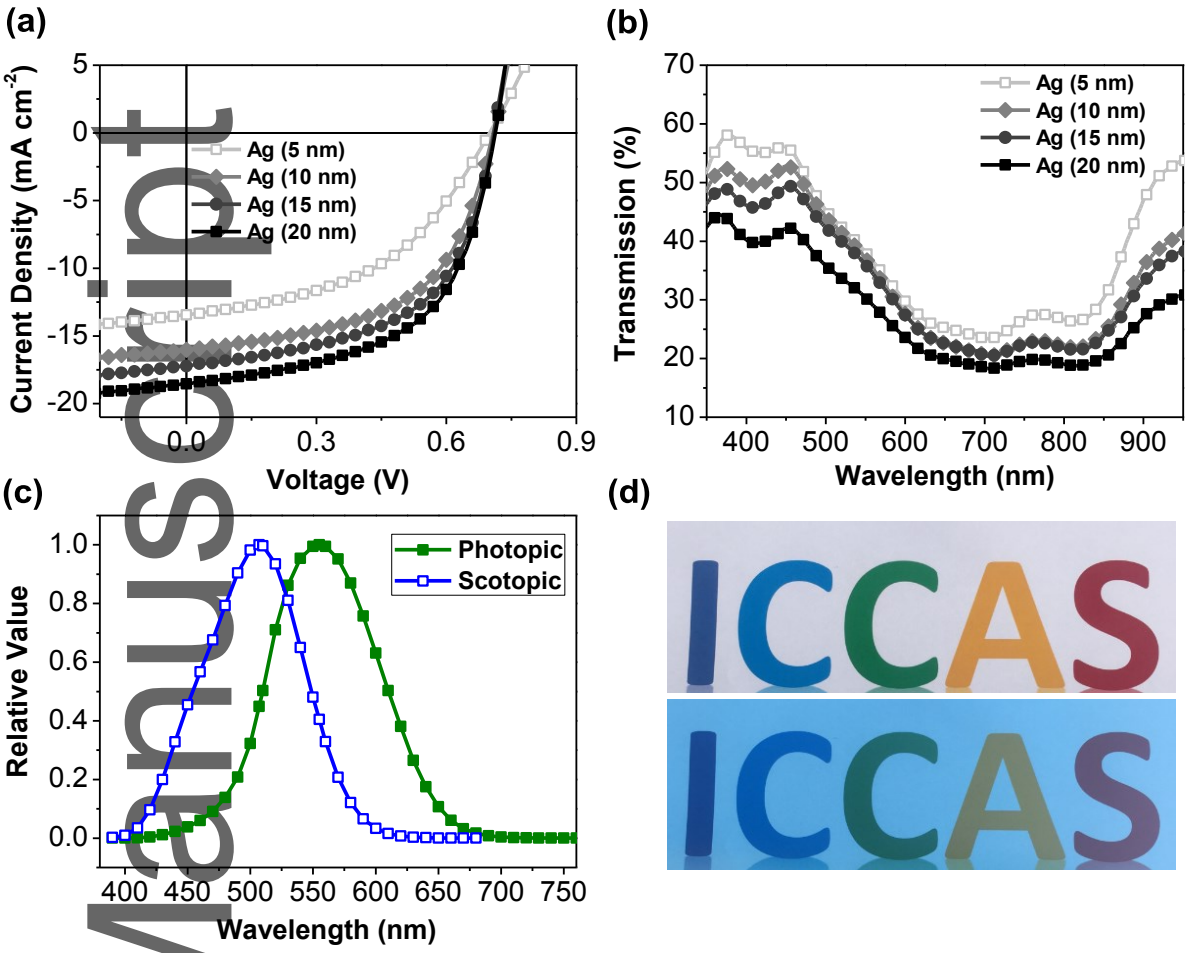

Figure 5. (a) Characteristic density vs voltage (*J*–*V*) curves and (b) the transmission spectra of the corresponding devices; (c) the standard human eye sensitivity spectra; (d) photographs of the institute abbreviation without and with the semitransparent device.

Table 1. Summarized photovoltaic parameters of the ATT-2-based inverted and semitransparent devices.

Cathode	additive	V_{oc} [V]	J_{sc} [mA cm^{-2}]	FF [%]	PCE [%]

MoO_3/Ag(100 nm)	NO	0.74	12.85	50	4.87(4.71)[a)]
MoO_3/Ag(100 nm)	2% CN	0.73	20.75	63	9.58(9.39)[a)]
MoO_3/Ag(5 nm)	2% CN	0.700	13.38	47	4.40(4.32)[a)]
MoO_3/Ag(10 nm)	2% CN	0.708	16.01	55	6.30(6.14)[a)]
MoO_3/Ag(15 nm)	2% CN	0.710	17.23	57	7.02(6.88)[a)]
MoO_3/Ag(20 nm)	2% CN	0.712	18.53	59	7.74(7.53)[a)]

[a)]The average values are obtained from over eight devices and are shown in parenthesis.

A small-bandgap electron acceptor ATT-2 was designed and synthesized for semitransparent (ST) OPV applications. By combining the PTB7-Th donor, the PCEs reached 9.58% for opaque devices and 7.74% for the STOPVs. The highest PCE among single-junction STOPVs could be attributed to the beneficial complementary NIR absorption of the low-bandgap donor and small-bandgap acceptor. Non-fullerene acceptors are thus very promising for the development of high-performance STOPVs.

Keywords: semitransparent organic solar cell, near infrared, non-fullerene acceptor, power conversion efficiency, thieno[3,4-*b*]thiophene

Feng Liu, Zichun Zhou, Cheng Zhang, Jianyun Zhang, Qin Hu, Thomas Vergot, Feng Liu,* Thomas P. Russell, and Xiaozhang Zhu*

Efficient Semitransparent Solar Cells with High NIR Responsiveness Enabled by a Small-Bandgap Electron Acceptor

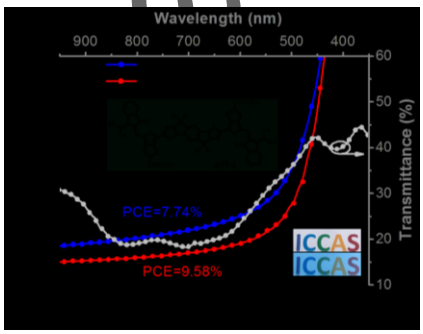

Submitted to ADVANCED MATERIALS

Supporting Information

for *Adv. Mater.*, DOI: 10.1002/adma.((please add manuscript number))

Efficient Semitransparent Solar Cells with High NIR Responsiveness Enabled by a Small-Bandgap Electron Acceptor

Feng Liu, Zichun Zhou, Cheng Zhang, Jianyun Zhang, Qin Hu, Thomas Vergot, Feng Liu, Thomas P. Russell, and Xiaozhang Zhu**

Materials

All the reactions dealing with air- or moisture-sensitive compounds were carried out in a dry reaction vessel under a positive pressure of nitrogen. (4,4,9,9-Tetrakis(4-hexylphenyl)-4,9-dihydro-*s*-indaceno[1,2-*b*:5,6-*b'*]dithiophene-2,7-diyl)bis(trimethylstannane) (**2**) were bought from Derthon Optoelectronic Materials Science Technology Co. LTD.. PTB7-Th were obtained from 1-Material Chem-scitech Inc.. PTB7-Th were obtained from 1-Material Chem-scitech Inc.. Unless otherwise stated, starting materials were obtained from Adamas, Aldrich, and J&K and were used without any further purification. Toluene was distilled over Na/benzophenone prior to use. Octyl 6-bromo-4-formylthieno[3,4-b]thiophene-2-carboxylate (**1**) was prepared according to the published procedures (Chen, Y.-C.; Chou, H.-H.; Tsai, M. C.; Chen, S.-Y.; Lin, J. T.; Yao, C.-F.; Chen, K. *Chem. Eur. J.* **2012**, *18*, 5430.).

Measurements

Hydrogen nuclear magnetic resonance (^{1}H NMR) and carbon nuclear magnetic resonance

(^{13}C NMR) spectra were measured on BRUKER DMX 400 spectrometers. Chemical shifts for hydrogens are reported in parts per million (ppm, δ scale) downfield from tetramethylsilane and are referenced to the residual protons in the NMR solvent ($CDCl_3$: δ 7.26). ^{13}C NMR spectra were recorded at 100 MHz. Chemical shifts for carbons are reported in parts per million (ppm, δ scale) downfield from tetramethylsilane and are referenced to the carbon resonance of the solvent ($CDCl_3$: δ 77.0). The data are presented as follows: chemical shift, multiplicity (s = singlet, d = doublet, t = triplet, m = multiplet and/or multiple resonances, br = broad), coupling constant in Hertz (Hz), and integration. MALDI-TOF measurements were performed on an Applied Biosystems 4700 Proteomics Analyzer. Elemental analyses were measured on a Carlo Erba 1106 elemental analyzer. UV-vis spectra were recorded on a JASCO V-570 spectrometer. Cyclic voltammetry (CV) measurements were carried out on a CHI640C analyzer in a conventional three-electrode cell setup with glassy-carbon electrode as the working electrode, a platinum wire as the counter electrode, Ag/Ag^+ as the reference electrode and calibrated with ferrocene/ferrocenium (Fc/Fc^+) as an external potential marker in anhydrous CH_2Cl_2 solution containing 0.1 M tetrabutylammonium perchlorate (TBAP) as a supporting electrolyte under a nitrogen atmosphere at room temperature. All potentials were corrected against Fc/Fc^+. CV was measured with a scan rate of 100 mV/s. Thermogravimetric analysis (TGA) was performed on a Shimadzu DTG 60 instrument at a heating rate of 10 °C min^{-1} under a N_2 atmosphere with runs recorded from room temperature to 550 °C. Atomic force microscopy (AFM) images of the thin films were obtained on a NanoscopeIIIa AFM (Digital Instruments) operating in tapping mode. Transmission electron microscopy (TEM) was performed using a JEOL 2200FS instrument at 160 kV accelerating voltage.

GIWAXS

Grazing incidence X-ray scattering characterization of the thin films was performed at the Advanced Light Source on beamline 7.3.3, Lawrence Berkeley National Lab (LBNL). Thin film samples were spin-casted on to PEDOT:PSS covered SiO_2 wafers. The scattering signal was recorded on a 2D detector (Pilatus 2M) with a pixel size of 0.172 mm by 0.172 mm. The samples were ≈15 mm long in the direction of the beam path, and the detector was located at a distance of ≈300 mm from the sample center (distance calibrated using a silver behenate standard). The incidence angle of 0.16º was chosen which gave the optimized signal-to-background ratio. The

beam energy was 10 keV, operating at top-off mode. Typically, 30 s exposure time was used to collect diffraction signals. All GIXD experiments were done in helium atmosphere. The data was processed and analyzed using Nika software package.

Resonant Soft X-ray Scattering (R-SoXS)

R-SoXS was performed at beamline 11.0.1.2 Advanced Light Source, LBNL. Thin film samples were spin-casted on the top of the PEDOT:PSS covered SiO_2 wafers. After that, the BHJ composite films were spin-casted on the top of the SiO_2/PEDOT:PSS substrates under exactly the same conditions as those for the fabrication of solar cell devices. The BHJ thin film was then flown in water, and transferred to silicon nitride window. The scattering signals were collected in vacuum using Princeton Instrument PI-MTE CCD camera.

Fabrication of organic solar cells

PSCs were fabricated with the structures ITO/ZnO/PTB7-Th:ATT-2/MoO_3/Ag. The devices were fabricated using ITO-coated glass substrates (15 Ω sq^{-1}), which were cleaned with de-ionized water, acetone, and isopropyl alcohol in successive 20 min sonication steps applying a final 20 min oxygen plasma treatment to eliminate any remaining organic component. A thin layer (ca. 30 nm) of ZnO was first spin-coated on the pre-cleaned ITO-coated glass substrates at 3000 rpm from a ZnO precursor solution and then baked at 200°C for 30 min under ambient conditions. The substrates were then transferred into a nitrogen-filled glovebox. The active layer was spin-coated on the ZnO layer from 1 ml of chlorobenzene solution containing PTB7-Th (8 mg) and ATT-2 (14.4 mg). Solvent additive, 1- chloronaphthalene (CN), was used to improve the BHJ morphology. Thin layer of MoO_3 (5 nm) was deposited as the anode interlayer, and Ag with different thickness were deposited as the top electrode at a low evaporation speed of 0.2 Å s^{-1} under 10^{-5} Pa. The precise thicknesses of silver electrode were calibrated by AFM. The active area of the device was *ca.* 3 mm^2.

Device Characterization

The current density–voltage (*J*–*V*) characteristics of unencapsulated photovoltaic devices were measured under N_2 using a Keithley 2400 source meter. A 300 W xenon arc solar simulator (Oriel) with an AM 1.5 global filter operated at 100 mW cm^{-2} was used to simulate the AM 1.5G solar irradiation. The illumination intensity was corrected by using a silicon photodiode with a protective KG5 filter calibrated by the National Renewable Energy Laboratory (NREL). The

external quantum efficiency (EQE) was performed using certified IPCE equipment (Zolix Instruments, Inc, SolarCellScan100).

SCLC Mobility Measurements

Space charge-limited currents were tested in electron-only devices with a configuration of Al/PTB7-Th:ATT-2/Al and hole-only devices with a configuration of ITO/PEDOT:PSS/PTB7-Th:ATT-2/MnO_3/Al. The devices were prepared following the same procedure described in the experimental section for photovoltaic devices, except for the metal electrode. The mobilities were determined by fitting the dark current to the model of a single carrier SCLC current with field dependent mobility, which is described as

$$J = \frac{9\varepsilon_0\varepsilon_r\mu_0 V^2}{8L^3} \qquad (1)$$

Where J is the current, μ_0 is the zero-field mobility, ε_0 is the permittivity of free space, ε_r is the relative permittivity of the material, V is the effective voltage, and L is the thickness of the active layer.

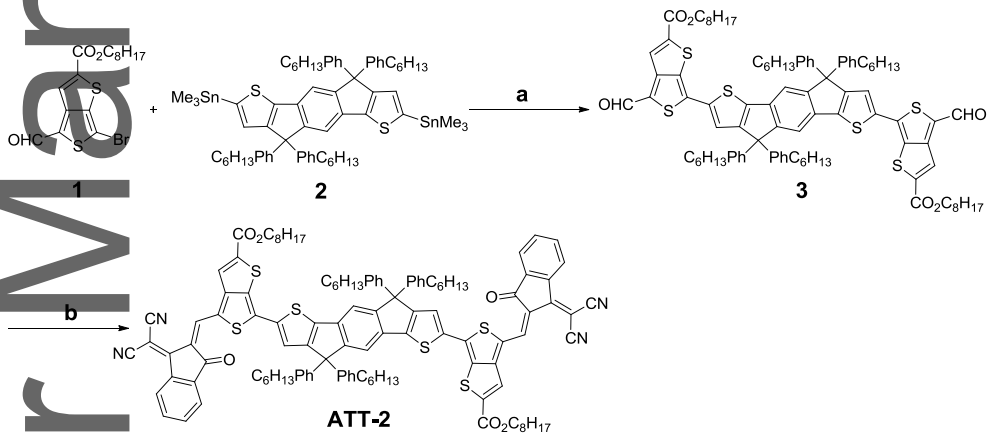

The reaction conditions were (a) $Pd(PPh_3)_4$, toluene, reflux; (b) 3-(dicyanomethylidene)indan-1-one, pyridine, chloroform, reflux.

Synthesis of compound 3: Octyl 6-bromo-4-formylthieno[3,4-b]thiophene-2-carboxylate **1** (177 mg, 0.44 mmol) and (4,4,9,9-tetrakis(4-hexylphenyl)-4,9-dihydro-s-indaceno[1,2-*b*:5,6-*b'*]dithiophene-2,7-diyl)bis(trimethylstannane) **2** (247 mg, 0.2 mmol) were dissolved in anhydrous toluene (4 mL) under nitrogen atmosphere, to which $Pd(PPh_3)_4$ (23 mg, 0.02 mmol) was added. The reaction was stirred and refluxed for 24 h under dark. The reaction mixture was filtered and washed with chloroform. The combined filtrates were concentrated under reduced

pressure and purified on a silica-gel column chromatograph to give 258 mg of compound **3** in 83% yield as a dark-red solid. ^{1}H NMR (400 MHz, $CDCl_3$): δ 10.01 (s, 2H), 8.11 (s, 2H), 7.50 (s, 2H), 7.39 (s, 2H), 7.20 (d, ^{3}J = 8.0 Hz, 8H), 7.12 (d, ^{3}J = 8.4 Hz, 8H), 4.37 (t, ^{3}J = 7.2 Hz, 4H), 2.58 (t, ^{3}J = 8.0 Hz, 8H), 1.78–1.82 (m, 4H), 1.56–1.64 (m, 8H), 1.30–1.36 (m, 44H), 0.85-0.91 (m, 18H); ^{13}C NMR (100 MHz, $CDCl_3$): δ 179.19, 162.26, 157.75, 154.11, 149.58, 145.18, 144.23, 142.05, 140.89, 137.15, 136.57, 135.92, 135.27, 128.62, 127.77, 122.62, 122.35, 117.98, 66.46, 63.24, 35.57, 31.77, 31.69, 31.32, 29.69, 29.31, 29.18, 29.13, 28.59, 25.89, 22.63, 22.58, 14.08; HRMS (MALDI-TOF) Calcd for $C_{96}H_{110}O_6S_6$ $[M]^+$, 1550.6627; found, 1550.6624.

Synthesis of ATT-2: Compound **3** (155.0 mg, 0.1 mmol) and 2-(3-oxo-2,3-dihydroinden-1-ylidene)malononitrile (194 mg, 1.0 mmol) were dissolved in chloroform (6 ml). 1 drop of pyridine was then added and the mixture stirred and refluxed overnight. The resulting mixture was extracted with chloroform, washed with water, and dried over $MgSO_4$. After removal the solvent, the crude product was purified on a silica-gel column chromatography to afford 160 mg of compound **ATT-2** in 84% yield as a dark-green solid. ^{1}H NMR (400 MHz, $CDCl_3$): δ 9.27 (s, 2H), 8.66 (d, ^{3}J = 8.0 Hz, 2H), 8.11 (s, 2H), 7.87 (d, ^{3}J = 6.8 Hz, 2H), 7.67–7.72 (m, 4H), 7.65 (s, 2H), 7.58 (s, 2H), 7.21 (d, ^{3}J = 8.1 Hz, 8H), 7.14 (d, ^{3}J = 8.1 Hz, 8H), 4.38 (t, ^{3}J = 5.4 Hz, 4H), 2.60 (t, ^{3}J = 7.8 Hz, 8H), 1.77–1.83 (m, 4H), 1.58–1.65 (m, 8H), 1.26–1.47 (m, 44H), 0.85–0.92 (m, 18H); ^{13}C NMR (101 MHz, $CDCl_3$) δ 188.84, 161.91, 159.55, 159.05, 157.39, 154.90, 147.14, 145.59, 142.76, 142.26, 140.61, 140.10, 137.78, 136.60, 136.34, 135.77, 134.89, 134.04, 132.06, 128.78, 127.83, 125.96, 125.08, 124.51, 123.32, 122.96, 120.11, 118.43, 115.43, 114.79, 68.18, 66.56, 63.33, 35.61, 31.81, 31.72, 31.35, 29.20, 29.16, 29.12, 28.60, 25.85, 22.66, 22.59, 14.09; HRMS (MALDI-TOF) Calcd for $C_{120}H_{118}N_4O_6S_6$ $[M]^+$, 1902.7376; found, 1902.7372; Anal. Calcd for $C_{120}H_{118}N_4O_6S_6$ (%):C, 75.67; H, 6.24; N, 2.94; Found (%): C, 75.52; H, 6.37; N, 2.91.

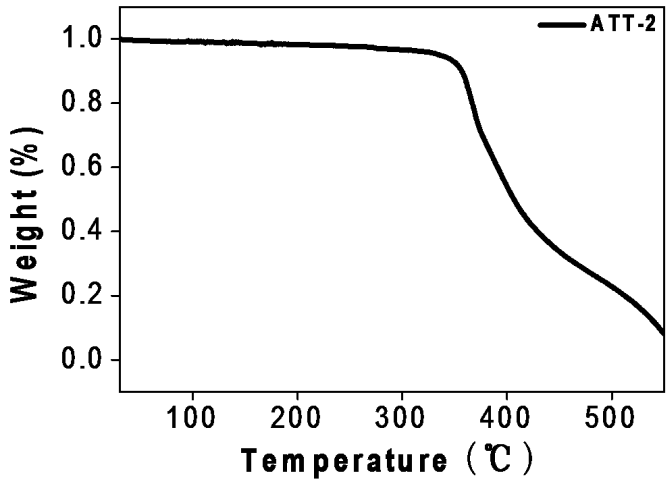

Figure S1. Thermal gravimetric analysis curve of ATT-2.

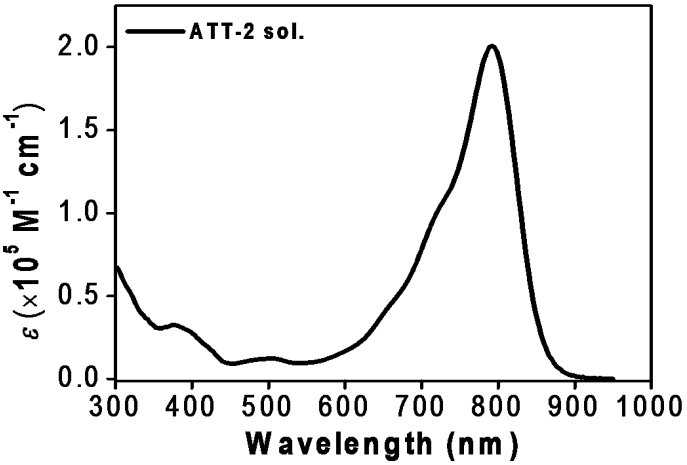

Figure S2. UV-Vis-NIR absorption spectra of ATT-2 in chloroform.

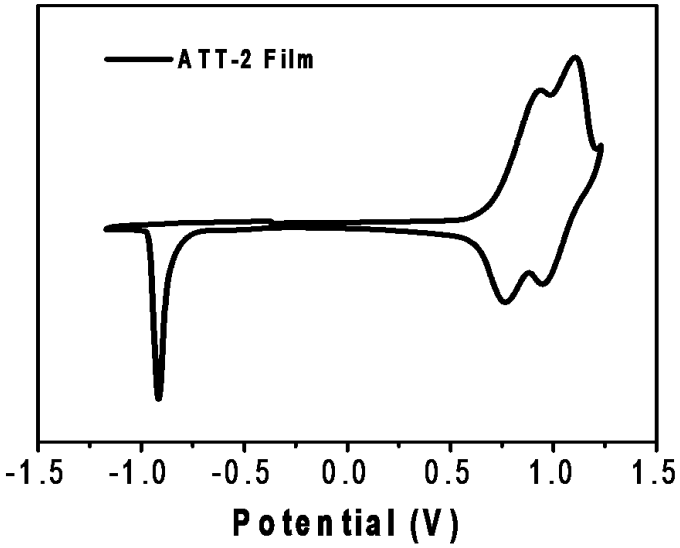

Figure S3. Cyclic voltammogram ATT-2 film in 0.1 M *n*-Bu_4NClO_4 MeCN solution (calibrated by Fc/Fc^+).

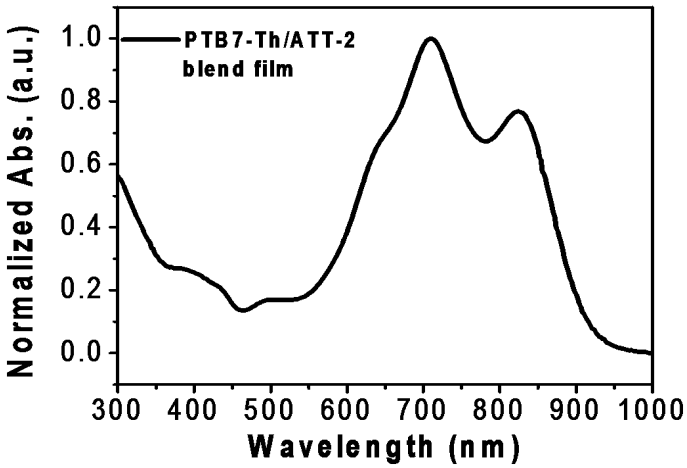

Figure S4. UV-Vis-NIR absorption spectra of ATT-2 and PTB7-Th blend film.

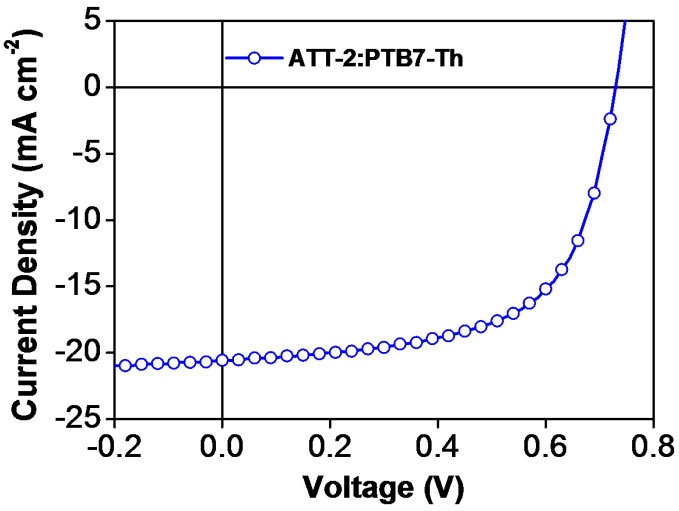

Figure S5. The *J-V* curve of the devices with active area of 0.1 cm².

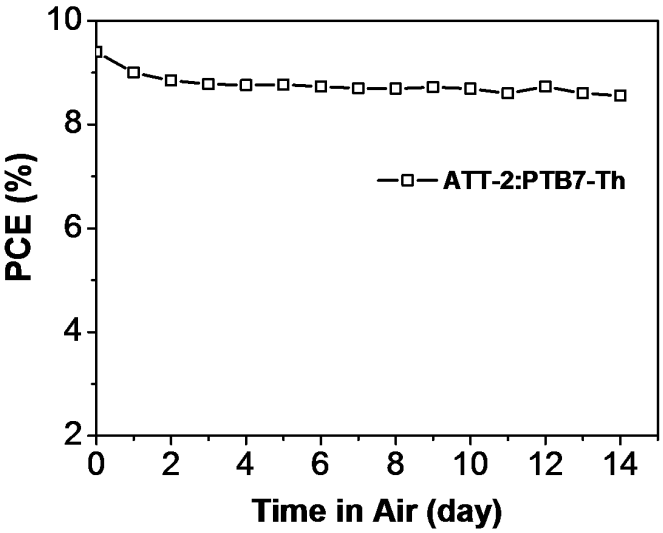

Figure S6. The stability of ATT-2:PTB7-Th device efficiencies in ambient conditions.

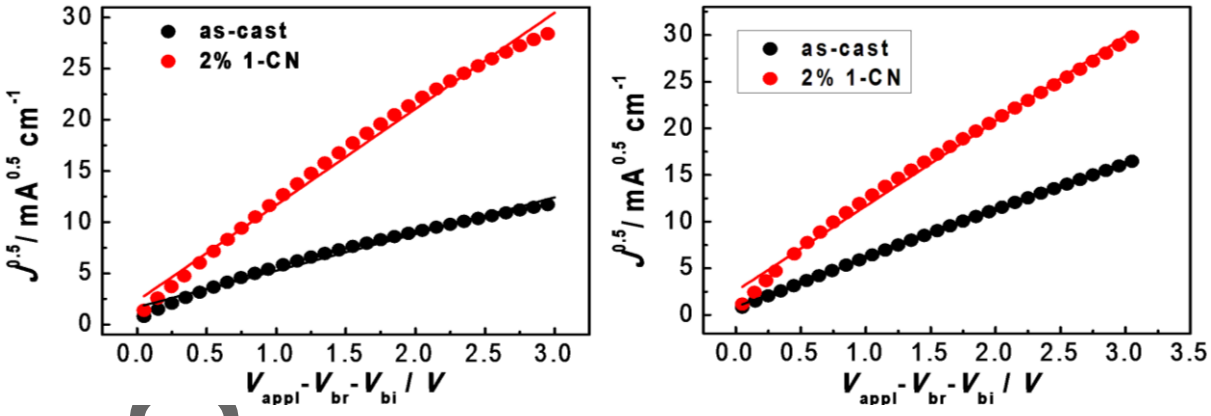

Figure S7. The hole mobility (left) and electron mobility (right) of PTB7-Th:ATT-2 blend films with or without 1-CN at their best OSC device characters measured by SCLC method.

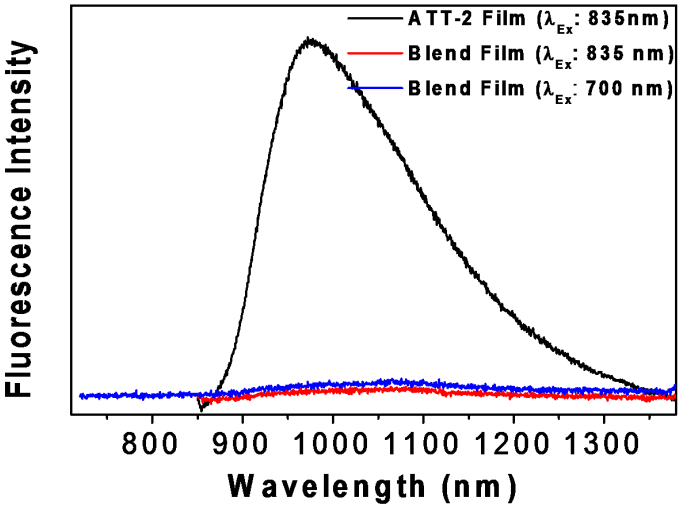

Figure S8. The steady-state PL spectra of the neat ATT-2 film(excited at 835 nm) and the blend film of ATT-2:PTB7-Th (excited at 700 nm and 835 nm, respectively).

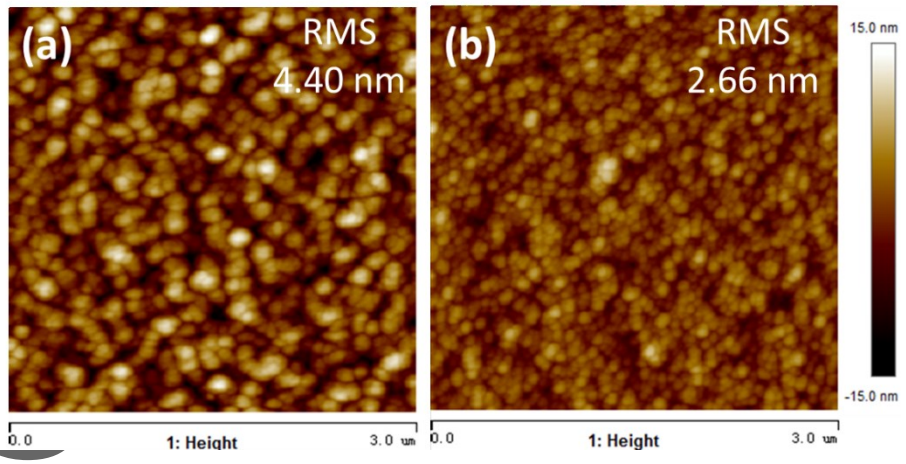

Figure S9. AFM height images of optimized PTB7-Th/ATT-2 blend films without (a) or with (b) 2% 1-CN as additives.

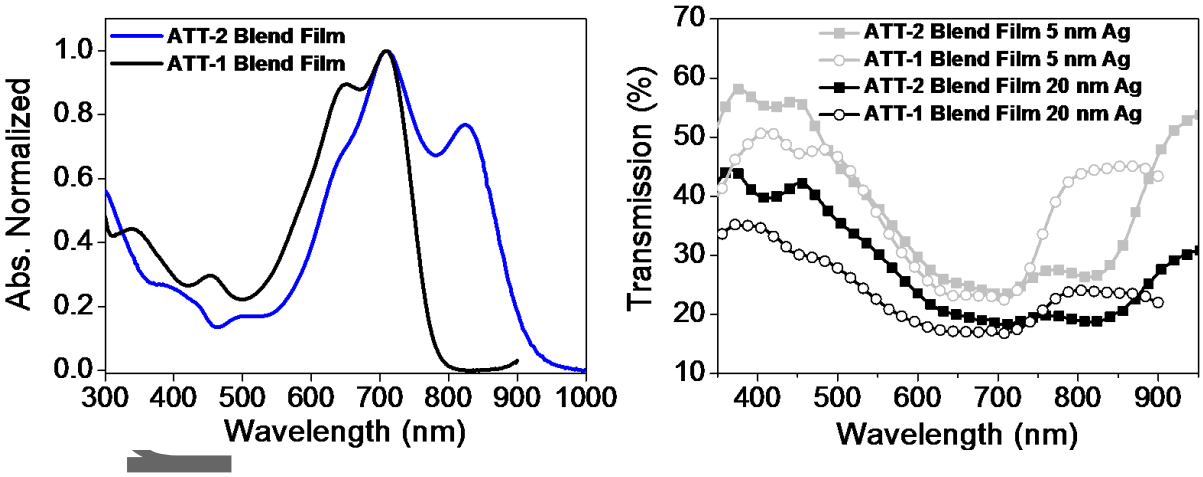

Figure S10. (a) The absorption spectra of ATT-2:PTB7-Th and ATT-1:PTB7-Th blend films. (b) The transmission spectra of the ATT-2:PTB7-Th and ATT-1:PTB7-Th blend films with Ag electrodes of different thicknesses.

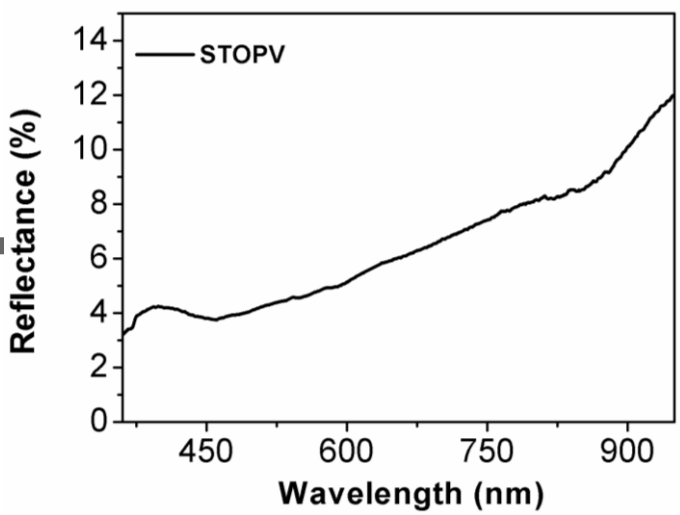

Figure S11. The reflection spectrum of the ATT-2:PTB7-Th-based STOPV.

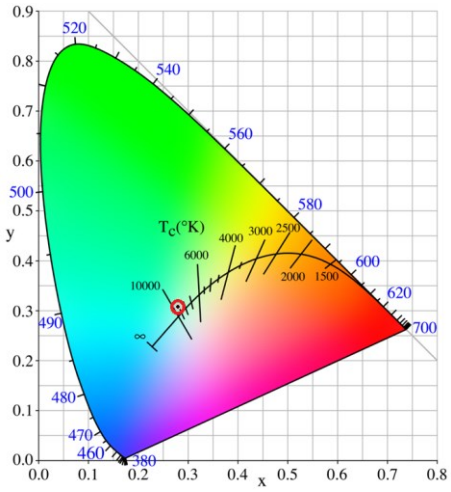

Figure S12. The color coordinates of the STOPV under AM 1.5G illumination on the CIE chromaticity diagram.

Dioctyl 6,6'-(4,4,9,9-tetrakis(4-hexylphenyl)-4,9-dihydro-*s*-indaceno[1,2-*b*:5,6-*b*']dithiophene-2,7-diyl)bis(4-formylthieno[3,4-*b*]thiophene-2-carboxylate) (3)

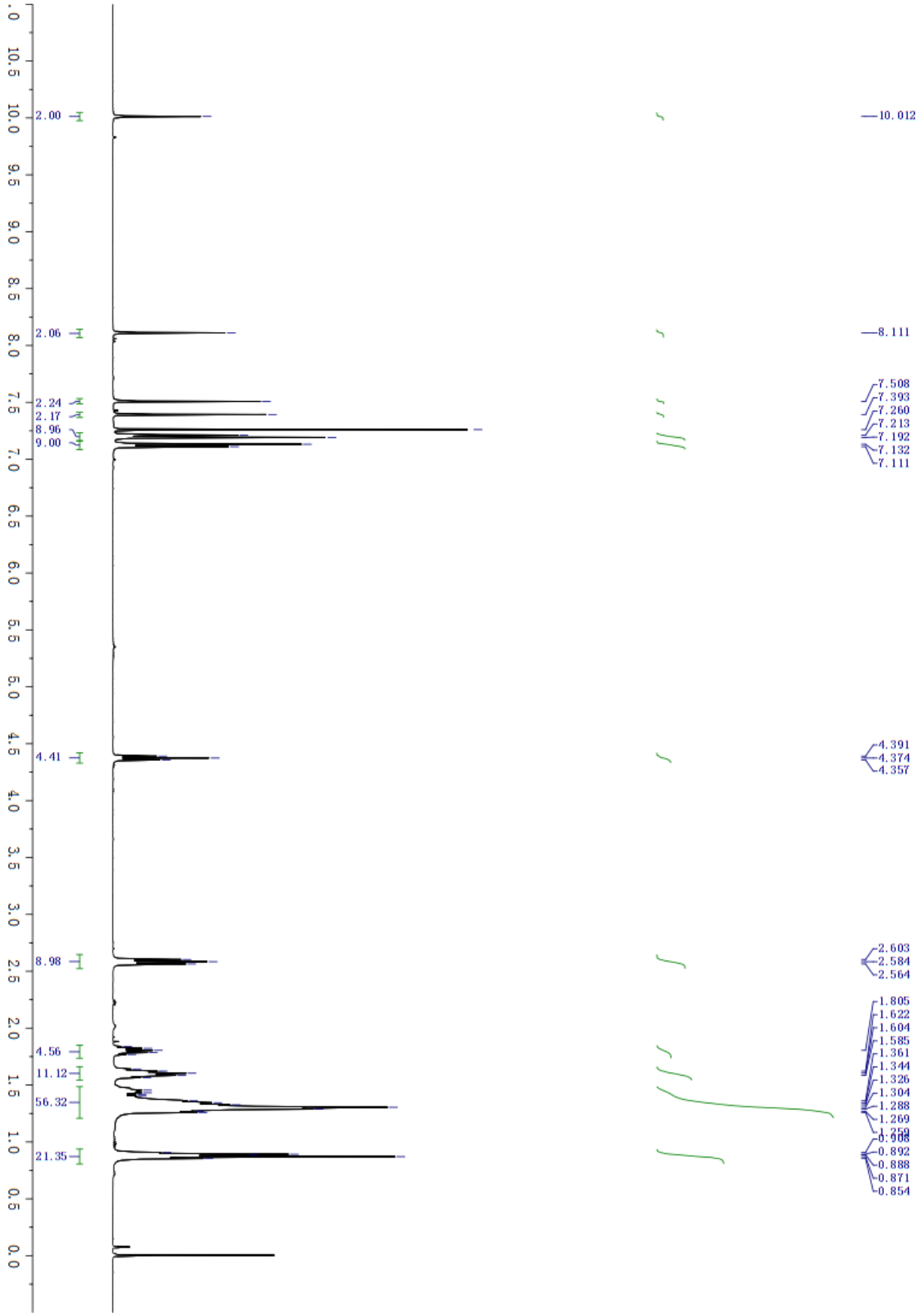

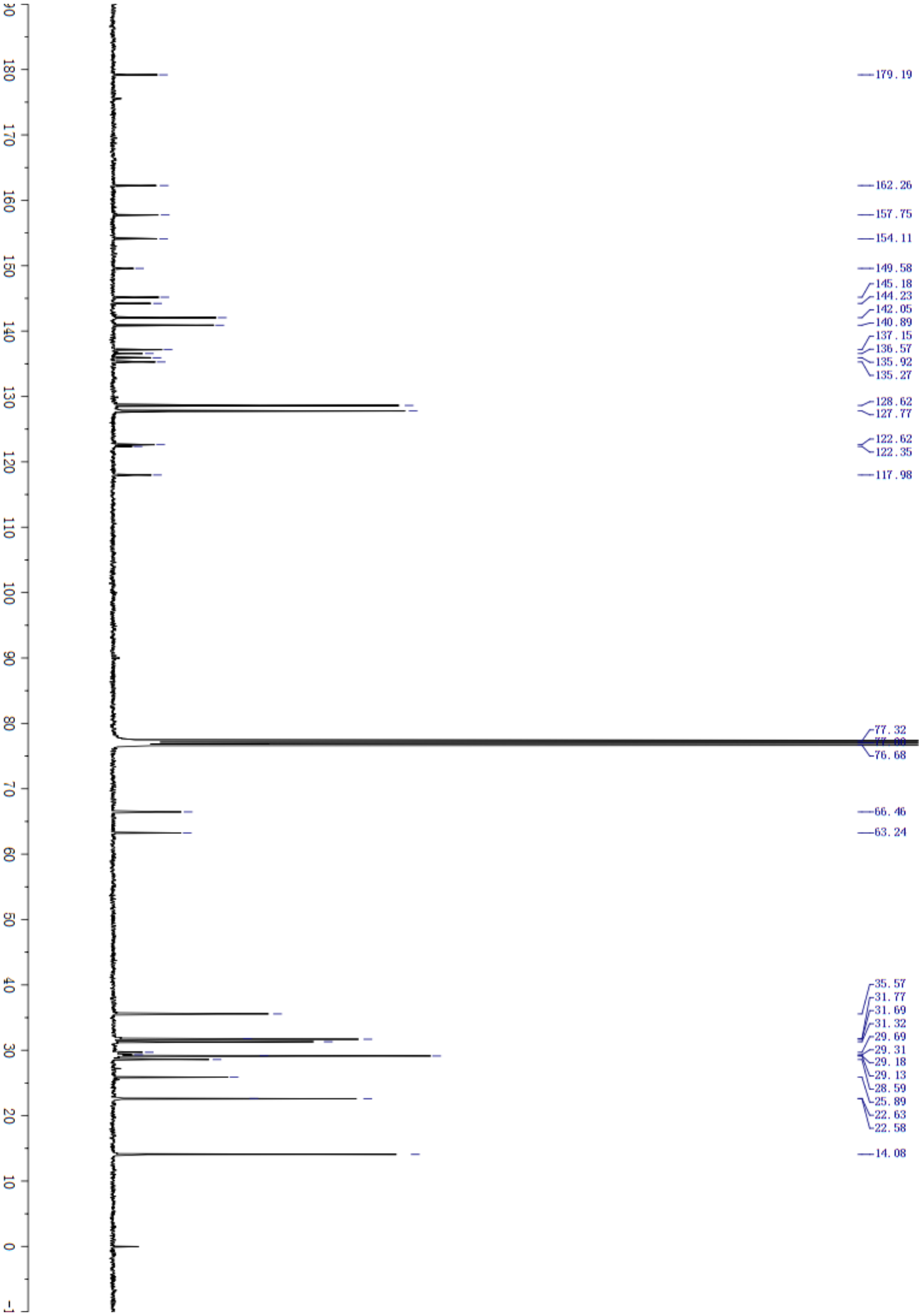

Dioctyl 6,6'-(4,4,9,9-tetrakis(4-hexylphenyl)-4,9-dihydro-*s*-indaceno[1,2-*b*:5,6-*b*']dithiophene-2,7-diyl)bis(4-((*Z*)-(1-(dicyanomethylene)-3-oxo-1*H*-inden-2(3*H*)-ylidene)methyl)thieno[3,4-b]thiophene-2-carboxylate) (ATT-2)